Energy Storage Materials 22 (2019) 450–460

Contents lists available at ScienceDirect

Energy Storage Materials

journal homepage: www.elsevier.com/locate/ensm

Roll to roll manufacturing of fast charging, mechanically robust 0D/2D nanolayered Si-graphene anode with well-interfaced and defect engineered structures

Biwei Deng [a,1], Rong Xu [b,1], Xiaokang Wang [b], Licong An [c], Kejie Zhao [b,**], Gary J. Cheng [a,c,*]

[a] School of Industrial Engineering, Purdue University, West Lafayette, IN, USA
[b] School of Mechanical Engineering, Purdue University, West Lafayette, IN, USA
[c] School of Materials Engineering, Purdue University, West Lafayette, IN, USA

ARTICLE INFO

Keywords:
Anode
Li-ion
Graphene-silicon

ABSTRACT

Silicon/graphene composite is a promising material for Li-ion battery anodes towards high energy/power densities and reliable performances. Tuning the nanostructure in silicon/graphene composite can lead to many desired properties, such as high capacity, high rate performance and good cycle stability. However, the silicon/graphene products of many existing approaches have many problems that are not fully resolved, including poor nanoscale uniformity, low mechanical strength, loose contacts and interfaces, low volumetric density and poor permeability of ions or electrolyte. These issues would cause the silicon/graphene anodes fail to deliver its best electrochemical performance. In this work, we report a layer-by-layer coated nanocomposite anode with well-integrated nanostructures, fabricated by a scalable laser shock assisted roll to roll deposition process. The nanocomposite anode consists of silicon nanoparticles (SiNPs) and reduced graphene oxide (RGO) sheets. The alternating SiNP and RGO nanolayers are compactly bonded with fine interfaces and wrapping effects after laser shock compression, resulting in higher mechanical strength of the overall electrode, without any binder addition. Moreover, highly dense nanoscale pores are found on the graphene sheets after laser shock compression and annealing, which help the infiltration of electrolyte and thus provides the extract channels for Li diffusion. The Si/RGO composite anode can deliver a high specific capacity of 1956 mAh/g at a high cyclic rate of 15 A/g and retain 71.3% of the initial capacity after 1000 cycles. This work provides a general methodology to fabricate layered 0D/2D nanostructures with well-interfaced and defect-engineered nanostructures for many applications in electro-optics, molecule sensing, and energy storage.

1. Introduction

Novel manufacturing processes for Li-ion battery electrodes (LIB) with high energy density and power density are in compelling need to meet the increasing standards of energy storage components in frontier applications like electric vehicles, renewable-energy power plants, etc [1]. As one of the promising anode materials, silicon delivers a theoretical capacity of 3579 mAh/g, which is around 10 times of the theoretical capacity of commercial graphite anodes, 372 mAh/g. However, directly using silicon, either in form of micro-scale powders or nanoparticles, in the conventional slurry process results in the products with poor performances [2–5]. The performance issues come from the poor intrinsic conductivity of silicon that causes low mass efficiencies, and the large volume change during electrochemical cycling that often leads to dramatic pulverization and rapid capacity decay [6,7]. Therefore, the next-generation manufacturing processes for silicon-based anodes need to generate well incorporated conductive matrix and mechanically reliable electrode structure for the long-term use [8–10].

Graphene is a light weight 2D material with the high electron conductivity and mechanical strength. The mechanically stable and highly conductive graphene can be used as a matrix to support active materials and further improve their electrochemical performance [11,12]. Therefore, combinations of graphene with silicon nanoparticles (SiNPs) would be effective to address the weaknesses of silicon-based anodes and thus

* Corresponding author. School of Industrial Engineering, Purdue University, West Lafayette, IN, USA.
** Corresponding author.
E-mail addresses: kjzhao@purdue.edu (K. Zhao), gjcheng@purdue.edu (G.J. Cheng).
[1] These authors contributed equally.

https://doi.org/10.1016/j.ensm.2019.07.019
Received 30 April 2019; Received in revised form 2 July 2019; Accepted 11 July 2019
Available online 17 July 2019

improve their electrochemical performance [13–18]. Recently, several methods have been developed to generate silicon/graphene composite anodes for LIB, such as vacuum infiltration [19–22], freeze drying of silicon/graphene suspensions [23,24], electrospray [16], dip coating [25] and various templated CVD methods [15,26–28]. However, many critical issues still exist for the fabrication of silicon/graphene composite electrodes by the existing methods. Firstly, randomly mixed graphene and SiNPs inevitably contains large agglomerates of SiNPs, which jeopardizes the uniformity of the silicon/graphene composite and causes further capacity loss [29]. Secondly, the high surface area of SiNPs requires a high weight ratio of inactive polymer binder (10–25%) [30,31], which significantly lowers the specific capacity and increases the cost of silicon/graphene composite electrodes. Without the polymer binder, it is difficult to ensure good interfaces between adjacent silicon particles (Si–Si) and between silicon and graphene (Si-G), which is crucial for both electrical conductivity and mechanical reliability of the electrode [30]. Thirdly, since perfect graphene sheets do not allow ions or electrolyte through, extra porosity is often necessary to allow sufficient electrolyte infiltration into the silicon/graphene composite electrodes, which inevitably lowers the volumetric capacity [32].

To address part of these challenges, additional processing steps have to be utilized prior to or during fabrication. For example, during vacuum infiltration or freeze drying, the surfaces of silicon or graphene are often modified in their liquid dispersions to induce self-assembly and further to improve the uniformity of the electrodes [19,33]. Aerosol process has been used to generate crumbled graphene that encapsulate SiNPs to enhance the silicon-graphene contact [34]. The van der Waals interfaces or introduced covalent bindings between silicon and graphene are proven to be effective in enhancing the overall performance of the anode [35,36]. Introducing in-plane vacancies on graphene sheets can improve the high-rate performance of the electrode since more ion pathways are provided [37]. Engineering the inner pores of graphene-silicon aerogels helps the internal electrolyte infiltration and thus improve the electrode performances [38]. Although these additional processing steps can partially solve those challenges in the fabrication of silicon/graphene electrodes, to the best of the authors' knowledge, there is yet no scalable processing methods that can fabricate a uniform, compact, mechanically reliable silicon/graphene composite electrode with well-contacted Si-G and Si–Si interfaces.

In this work, we presented a scalable manufacturing method for obtaining layer-by-layer silicon/reduced graphene oxide (Si/RGO) composite anode with post laser-shock (LS) compression treatment to improve the nanoscale interfaces within the electrode. The layer-by-layer configuration with reduced graphene oxide (RGO) and SiNPs is a direct result from alternate gravure roller printing. It ensures the uniform composition of the electrode down to the nanoscale and the layer-structured distribution of the two components. Further LS compression compacted and strengthened the electrode, while improving the Si–Si and Si-G interfaces within and between the silicon and graphene nanolayers. Compared to low-strain rate compression techniques, LS compression provides strain rate of $\sim 10^6\ s^{-1}$, which is particularly effective to form well-integrated nanostructures in the Si/RGO nanolayers. We discover that LS compressed Si/RGO composite shows conformal wrapping of graphene on silicon nanoparticles. In this scenario, no further adhesive binder is needed, which increases the energy density and meanwhile lowers the cost of the Si/RGO composite. Interestingly, the strain induced in graphene sheets results in highly dense nanoscale pores after furnace annealing. These nano-pores could act as the internal electrolyte and ion pathways in the composite electrode. As a result, the final Si/RGO composite anodes show an outstanding capacity of 1956 mAh/g at a very high current density of 15 A/g. The LS compressed electrodes show higher rate performance than its control samples without LS. The high capacity at high current density is able to retain 71.3% after 1000 cycles.

2. Results and discussion

2.1. Laser-shock (LS) compressed layer-by-layer Si/RGO anodes

In aim of compatibility to the industry-level roll-to-roll coating process, a lab-level roll-to-roll gravure roller coating process is used to prepare the layer-by-layer Si/RGO electrodes. As shown in the process schematics of Fig. 1a, SiNP dispersion of 4 mg/mL and graphene oxide (GO) dispersion of 1.5 mg/mL are alternatively coated on a copper foil. The coating process consists of a number of coating/drying cycles. The mass loading of the electrode is controlled by the number of coating/drying cycles. Since the GO sheet in the dispersion will stack up upon drying, they will form a mechanically robust film that supports the SiNP layer in between. Photos of the prepared dispersions, coating equipment and the as-coated Si/RGO composite electrode sheet is shown in Fig. 1b–d. After the coating process is done, the Si/RGO composite electrode are transferred to the LS compression process followed by furnace annealing for the final product. The demonstrated processing sequence is compatible with the roll-to-roll coating and laser processing system in Fig. S1.

As shown schematically in Fig. 1e and f, the merits from LS compression are i) compaction of the electrodes, ii) enhancement of the nano-scale interfaces between Si–Si and Si-G. Ideally, in a Si/RGO composite anode, the contact between SiNPs and graphene is crucial for the electron transport from graphene to SiNPs or from lithiated SiNPs to graphene. In the meantime, these contact spots between SiNPs and graphene sheets are separated and distributed throughout the electrode. Compared to continuous interfaces between graphene and larger Si particles or Si films, which might suffer from fracture due to the volume expansion of Si, the separated and distributed nanoscale contact spots could allow the electrode matrix for higher cycle life. Because there are extra room between SiNPs and graphene sheets, which could help relax the stress caused by volume expansion despite the tight bonding. On the other hand, deformation induced defects or pores help the Li ions to pass through graphene instead of travelling around the graphene edges, hence shortening the ion diffusion length during charge/discharge. As a result, an augmented high rate performance is expected from the LS compressed Si/RGO composite electrode.

Fig. 2a shows the cross-sectional view of the layer-by-layer Si/RGO composite electrode before and after LS compression process. Before LS compression, the Si/RGO composite electrode is often prone to delamination. Because of the lesser contact between SiNPs and graphene, whose formation is only driven by the capillary forces during drying of the solvents, the film easily falls apart (during cross-section cutting) to pieces of fragments. After LS compression, the treated Si/RGO composite electrode is more compact and thinner. Due to the improved contact between Si–Si and Si-G, the composite electrode is more mechanically integrated and robust, while Si/RGO fragments are absent when the electrode is cut. The improved internal contact between Si–Si and Si-G, which is likely dominated by van der Waals forces, ideally results in augmented effective mechanical strength of the composite electrode. It can be also measured that the thickness of the Si/RGO electrode also significantly reduced after LS process (from 7.3 μm to 4.4 μm). The 4.4 μm thick electrode consists of 80 layers of SiNPs and 81 layers of RGO. Assuming that the thickness of the RGO layer is negligible, since it closely complies with the shape of the SiNPs, the average thickness of each SiNP layer is approximately 55 nm. Considering that the average thickness of the SiNP layer after LS is comparable to the size of the SiNPs (50–80 nm), it can be inferred that the SiNP layers are initially loosely packed and are compressed to an interspersed manner.

To measure the mechanical strength change brought by the LS compression, we conducted nanoindentation test on the Si/RGO composite electrodes. The obtained modulus and hardness data are shown in Fig. 2b. Detailed comparison of the stress-strain curves obtained from the

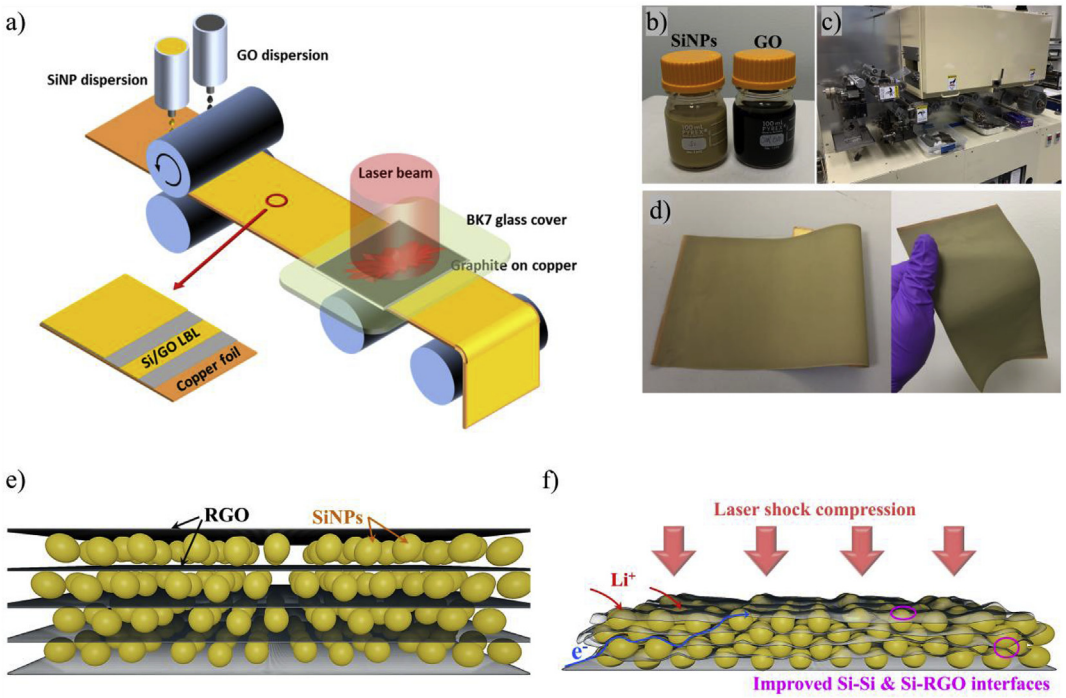

Fig. 1. a) Schematic of sheet-scale LS assisted manufacturing of layer-by-layer Si/RGO composite anode for Li-ion battery. Photographs of (a) SiNPs and GO dispersions, (b) roll-to-roll coater, and (d) as-coated Si/RGO composite electrode sheet. Schematics illustrating e) the loose SiNPs/graphene layer-by-layer structure before LS compression and f) the densely packed SiNPs encapsulated by large graphene sheets after LS compression.

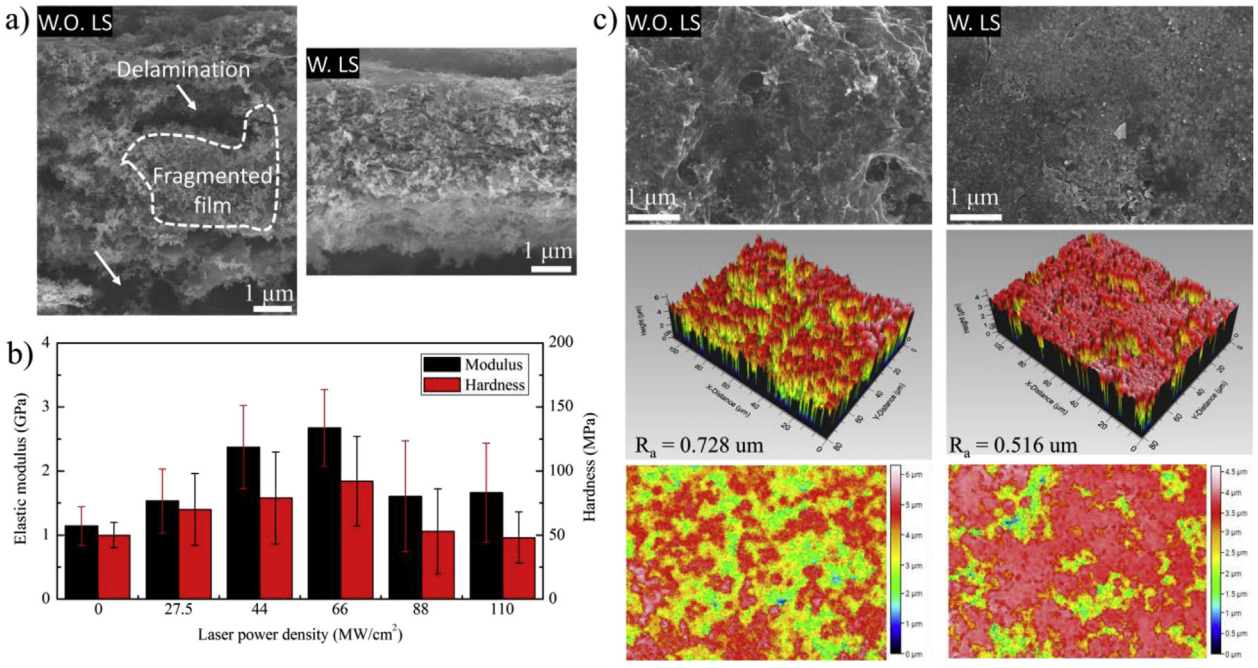

Fig. 2. a) Cross-sectional morphologies of the Si/RGO electrode before and after LS compression. Loading: 0.5 mg/cm^2 b) Modulus and hardness values of the Si/RGO composite electrode treated with LS compression of varied laser power. c) Surface morphologies of the Si/RGO electrode before and after LS compression.

nanoindentation testing are shown in Fig. S2. It is shown that as the laser power density increases from 0 to 66 MW/cm^2, the average modulus and hardness value monotonously increases. While as the laser power density increases from 66 MW/cm^2 to 110 MW/cm^2, the average modulus and hardness value decreases. This indicates that the ideal laser power density for LS compression process is nearest to 66 MW/cm^2 amongst all the power selections. When the laser power density is below this value, the induced shock pressure is beneficial to generating contact between the components in the Si/RGO composite and improve its mechanical integrity. When the laser power density is above 66 MW/cm^2, the shock pressure could be so high that it generates damages or bounce-backs that in turn diminish the overall mechanical property of the Si/RGO composite electrodes. The damage induced by high laser power density is also confirmed by the large discreteness of the mechanical strength in Fig. 2b.

Another significant improvement from the LS compression is on the surface condition of Si/RGO composite electrodes. As shown in Fig. 2c,

SEM images suggest that the surface roughness of the Si/RGO composite electrode significantly reduced after LS compression. The confocal microscope measurement using optical profilometer indicates that the surface roughness is 0.728 μm for the Si/RGO composite electrodes before the LS compression while is reduced to 0.516 μm after a LS compression with a power density of 66 MW/cm^2. However, the surface condition of Si/RGO composite electrodes does not show further improvement though the LS compression with a higher power density of 110 MW/cm^2 is applied (Fig. S3). The fact that excessive laser shock power couldn't further reduce the surface roughness can be attributed to two aspect. Firstly, the damage or bounce-backs generated by the laser shock of excessive power worsen the flattening effect. Secondly, excessive laser shock could induce adhesion between the copper sacrificial layer and the top surface of the electrode, which eventually causes loss of electrode materials and increase of roughness. Statistic information about the surface roughness of Si/RGO electrode after LS compression of varied power densities are presented in Table S1 of supporting information. Considering the change of mechanical properties and surface roughness of the electrode induced by varied LS power density, we selected 66 MW/cm^2 as the go-to laser power density for the following electrode processing.

The nanoscale morphology of the LS compressed layer-by-layer Si/RGO composite electrode is studied to unveil the arrangement of the nano-components within the matrix. Three characteristic nanostructures will be highlighted as the followings: 1) conformal graphene wrapping; 2) tight bonding between Si–Si and Si-G; 3) deformation induced graphene pores. Fig. 3a shows a typical morphology of non-LS treated Si/RGO composite, where graphene rests on SiNPs loosely, driven by the capillary forces during vaporization of solvents. The graphene layer only contacts several stood-out SiNPs, leaving out the majority of the SiNPs. On the contrary, shown in Fig. 3b, most SiNPs in a LS compressed Si/RGO composite electrode are well wrapped by the graphene layer. The graphene and SiNPs stay in close contact thanks to the Van de Waals forces at their interface, which balance out possible elastic strains. Fig. 3c&d show the comparison under TEM inspection between the Si/RGO composites before and after LS compression. For the non-LS treated Si/RGO composite (Fig. 3c), the area on the graphene where SiNPs detached from, shows nearly flat shape. This implies that the capillary force driven contact between SiNPs and graphene only impose elastic strains on graphene layer, which recover when SiNPs detach. On the other hand, the graphene layer in the LS compressed Si/RGO composite stays crumbled even after the SiNPs detachment (Fig. 3d) due to the local folding or plastic deformation occurred on the graphene layer during LS.

As shown in Fig. 3e&f the SiNPs can also be severely deformed by the LS. The originally spherical SiNP (Fig. 3e) is deformed to a dome shape, and tightly attaches to a graphene flake. More SiNPs deformed and attached to graphene sheets are shown in Fig. S4. Moreover, deformation twins are generated when two SiNPs collides during the LS compression (Fig. 3f & Fig. S5). The plastic deformation near the contact area between two SiNPs ensures better Si–Si contact. These joined SiNPs later stay connected after lithiation/delithation cycles, even when the individual SiNPs expand in volume and become mesoporous (Fig. 3g). It is worth noting that these SiNPs do not merge completely, leaving sufficient porosity within the matrix. These evidences prove that LS compression process is capable of imposing significant deformation in nanosized materials, in this case, graphene and SiNPs, and further inducing tight bonding between Si–Si and Si-G at nanoscale, while preserving necessary porosity in between. In addition, when graphene sheets are forced to wrap on the SiNPs, the strained area on the graphene sheets is often near the edges of the contact. The strain might assist the pre-existed crystalline defects on the graphene to develop into nanoscale pores, especially during the thermal annealing process. As shown in Fig. 3h, SEM observations support this mechanism, since the nanopores on the graphene sheets are only generated around the SiNPs, or in Fig. 3i, around the dimples on the graphene sheets. The TEM observation in Fig. 3j confirms that the pores are generated on the deformed graphene area, which is around the SiNPs. Ideally, these nanopores can exhibit as channel for Li ion transportation, while perfect graphene sheets won't allow Li ions to pass through. In summary, high energy LS compression induces better contact between Si–Si and Si-G, as well as nanopores on graphene sheets, thus allowing the binder-free Si/RGO composite electrode to maintain a good mechanical and electrochemical integrity.

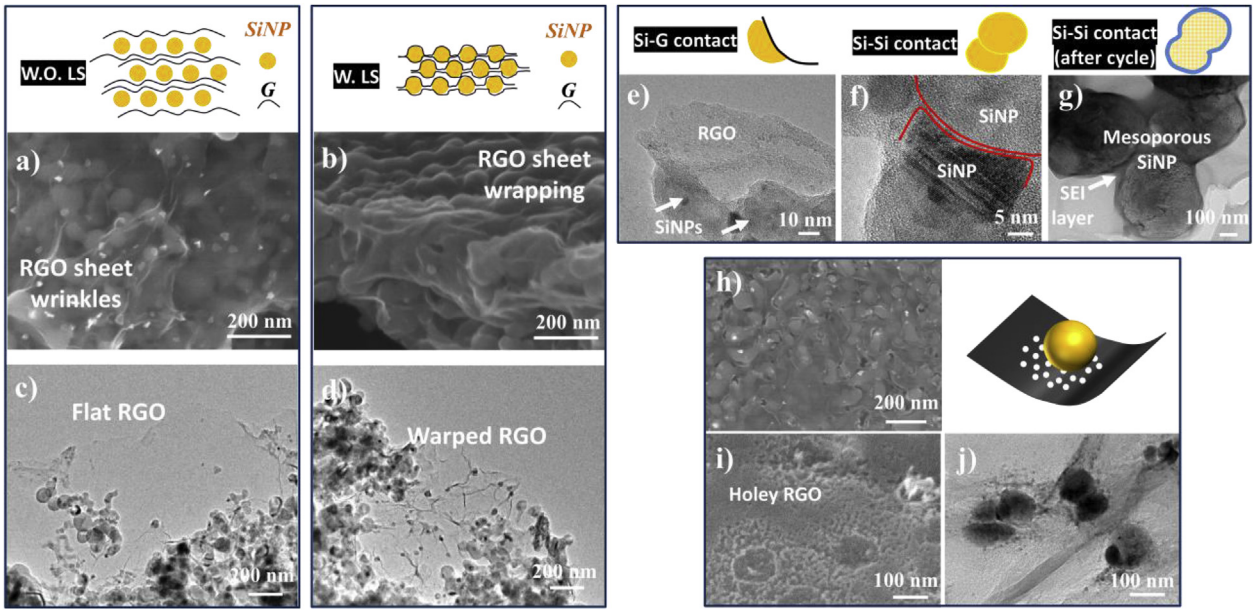

Fig. 3. a&c) The morphology of Si/RGO composite without LS compression in a) SEM and c) TEM, showing slight graphene wrinkling on SiNPs; b&d) The morphology of Si/RGO composite with LS compression in b) SEM and d) TEM, showing strong graphene wrapping on SiNPs. e) TEM observation of the deformed SiNP, tightly bonded to a graphene flake; f) TEM observation of the deformation twins in a SiNP induced by the collision between adjacent SiNPs during LS compression; g) The after-cycle morphology of LS compression joined SiNPs, showing that they stay joined despite becoming mesoporous after cyclic expansion/shrinkage; h) Deformation induced pores on the graphene layer loaded by SiNPs; i) The morphology of the graphene layer after SiNPs are etched out by KOH; j) TEM observation of the porous graphene sheets loaded by SiNPs.

Molecular dynamics modeling was performed to illustrate the effects of LS compression interaction between SiNPs and graphene layers. As shown schematically in Fig. 4a & Fig. S6, LS compression is performed to a composite structure, in which layers of SiNPs in hexagonal packing are sandwiched between monolayer graphene layers. Due to the computational cost, the diameter of the SiNPs is chosen to be 10 nm, while the gap between adjacent SiNPs is set to be 4 nm. The laser compression condition is set according to our previously published method [39,40], correlating laser shock pressure with the initial velocity of the impactor. We constructed two scenarios to model the interaction between Si–Si and Si-G respectively. The Si–Si scenario has three graphene layers and four SiNP layers; and the Si-G scenario has four graphene layers and three SiNP layers. Fig. 4b shows the joining of the SiNPs affected by propagated laser shock wave in the Si–Si scenario. Due to the nano-size effect, the crystallinity of the SiNPs near the colliding surface is compromised (marked in red in the right image of Fig. 4b), which further developed into cold welding of the nanoparticles. In the Si-G scenario, we can see from Fig. 4c that the graphene layer is conformally wrapping onto the SiNPs due to the high strain rate nanoshaping process during LS compression. This process ensures good interfaces between graphene and SiNPs. The cold integration between graphene and SiNP nanolayers by laser shock generates better contact by cold joining and wrapping throughout the composite structure, while the spatial arrangement of the initial nanostructure is preserved due to ultra-short deformation time. It is further revealed that the high strain rate laser compression significantly affected the pre-existed structural defects on the graphene layers. Fig. 4d shows the representative graphene layer with random structural defects before and after laser shock. It is observed that laser shock process is effectively 'opening' these defects by straining the surrounding areas. We use the area increasement of these imperfections as a measure of the strain effect. The histogram in Fig. 4e summarizes the imperfection counts by their area increasement on the selected graphene. 38.5% of them has area increases of over 50%. Considering that the area increase of an imperfection is closely related to its position on the graphene. The imperfections are then labeled with a position factor ($d/D_{1/2}$), which is derived by dividing the distance between the imperfection and the nearest projection of SiNP center on the graphene (d) by half of the distance between two adjacent projections of SiNP centers on the graphene ($D_{1/2}$) (Fig. S7). It is shown in Fig. 4f that when the position factor is smaller than 1, the imperfection size after laser shock is acutely affected by their position factors. When the imperfection is nearer to the projection of SiNP center on graphene, the size enlargement is more significant. On the other hand, when the position factor is larger than 1, the imperfection size after laser shock is often close to its original value. This phenomenon is supported by our experimental observation in Fig. 3i, in which larger pores are nearer the dimple generated by SiNPs, while smaller powers are farther away; when the location is too far from any dimple, the imperfection become invisible in SEM observation. Thermodynamics of Li insertion and extraction in the defected graphene has been well studied in the literatures via first-principle calculations [32,41]. It is evident that lithiation is not favorable in pristine graphene while an enhanced Li adsorption is induced on defective graphene, partially because of the increased charge transfer between adatom and underlying defective sheet. These imperfection sites could serve as the energetically favorable places to accommodate the insertion of Li. Further out-of-plane transportation of Li ions could be enabled by these imperfection sites as their sizes become sufficiently large.

2.2. Electrochemical performance of the Si/RGO nanocomposite electrode

Electrochemical performance of the Si/RGO nanocomposite electrode is characterized using half-cells. Si/RGO composite electrodes with mass loadings ranging from 0.1 mg/cm^2 to 1.0 mg/cm^2 are cycled at the charge/discharge rate of 6 A/g (Fig. 5a). Typically, the capacity of the Si/RGO electrode first increases during the first few tens of cycles, then decreases in the later cycles. The initial increase of capacity can be explained by the gradual activation of silicon. This phenomenon has been reported when nano-silicon is used as the anode [10,42]. The decay of the capacity can be attributed to the continuous and irreversible solid electrolyte interface (SEI) layer formation. The maximum specific

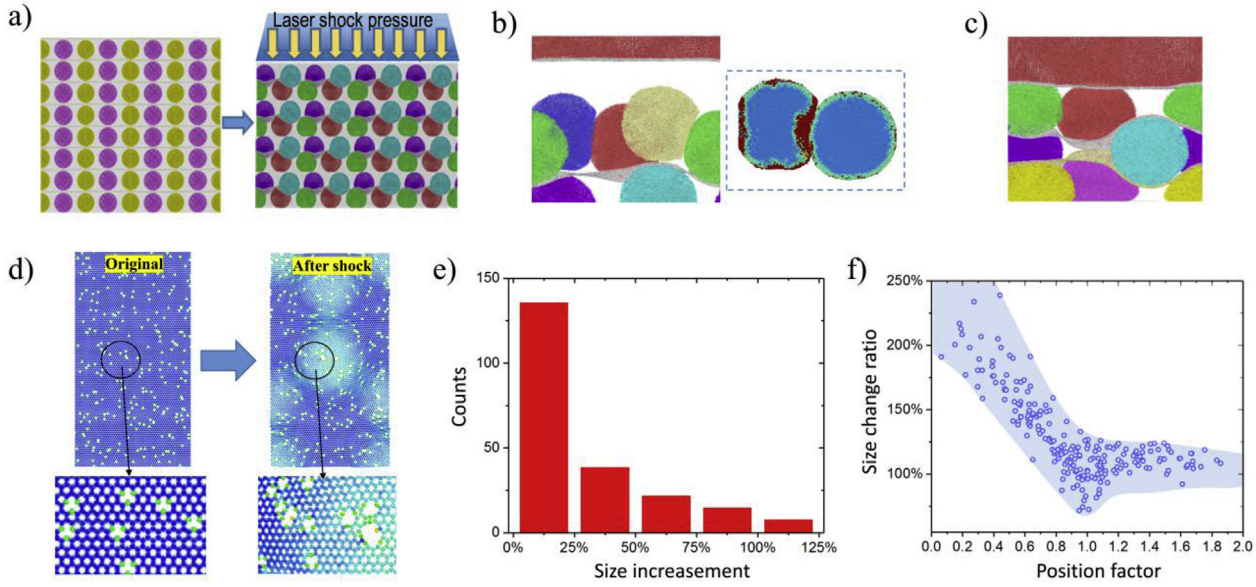

Fig. 4. a) Schematic of laser shock compression of the SiNP and defect graphene layered structure in MD modeling; b) Morphology of joining of adjacent SiNPs accelerated by laser shock wave. Atoms marked in red is the right image are the atoms that no longer comply with diamond crystal structure. c) Morphology of graphene conformally wrapping onto the SiNPs driven by laser shock compression. d) Representative graphene layer with pre-spread imperfections, which is deformed by the upper and lower SiNP layers. Zoom-in views shows the size of the imperfections before and after laser shock. e) Size increasement distribution of the imperfections on the representative graphene layer. f) Relationship between size change ratio and position of the imperfections on graphene. Position factor ($d/D_{1/2}$) is used to label the location of the imperfections. Here d is the distance between the imperfection and the nearest projection of SiNP center on the graphene, and $D_{1/2}$ is half of the distance between two adjacent projections of SiNP centers on the graphene. (For interpretation of the references to color in this figure legend, the reader is referred to the Web version of this article.)

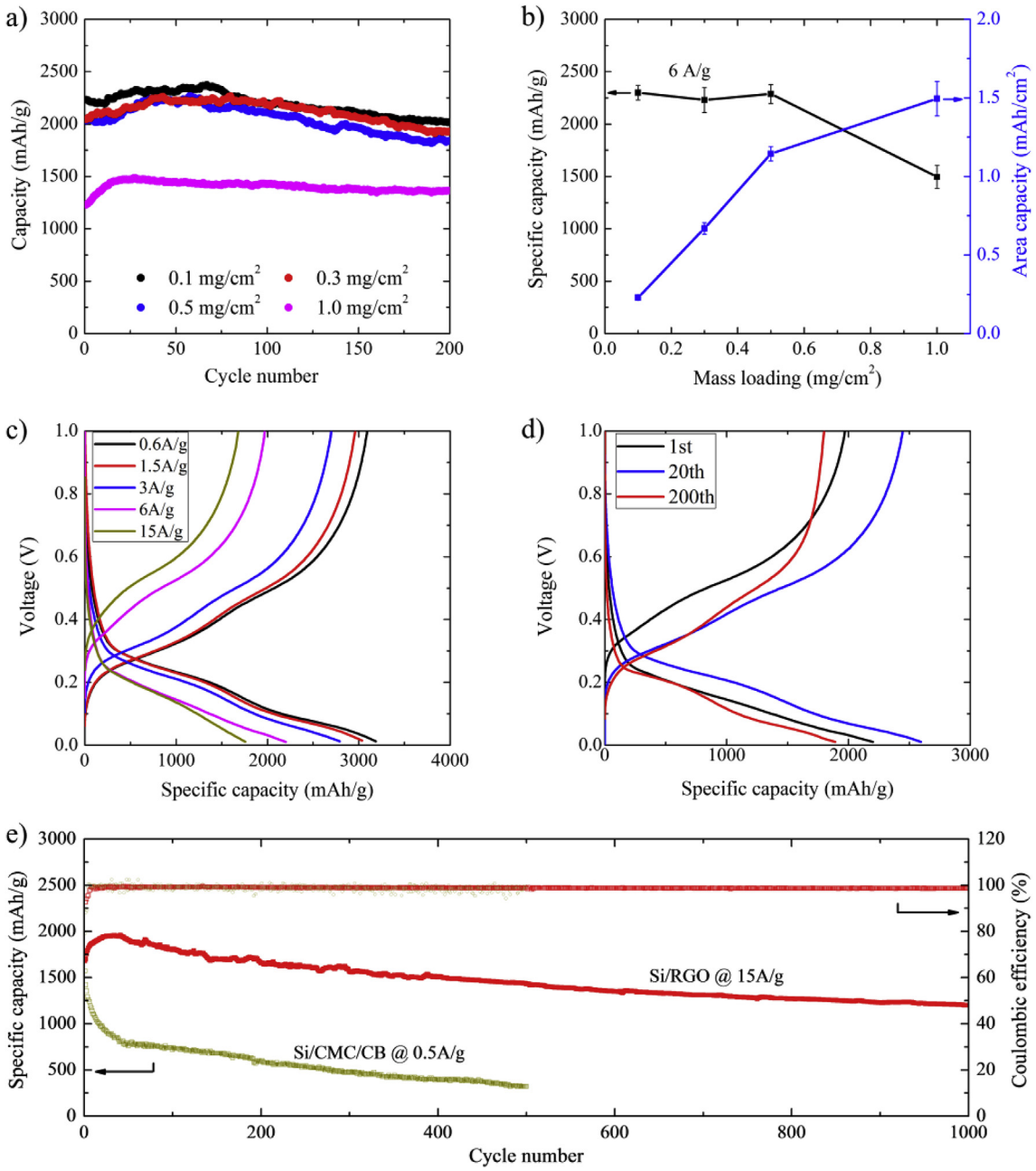

Fig. 5. Electrochemical performance of the Si/RGO composite electrode. a) cycling performance of Si/RGO composite electrodes with mass loadings ranging from 0.1 mg/cm^2 to 1.0 mg/cm^2. The half-cells are cycled at the charge/discharge rate of 6 A/g and in a voltage range between 0.01 and 1.0 V. b) The maximum specific capacity (black) and the corresponding areal capacity (blue) of the Si/RGO composite electrode in terms of mass loading. c) Galvanostatic charge/discharge curves at different cyclic rates in a voltage range between 0.01 and 1.0 V. d) Galvanostatic charge/discharge curves at 1st, 20th and 200th cycles for a cyclic rate of 6 Ah/g. e) Long-term cycling performance of Si/RGO composite electrode cycled at a charge/discharge rate of 15 Ah/g. (For interpretation of the references to color in this figure legend, the reader is referred to the Web version of this article.)

capacity (black) and the corresponding areal capacity (blue) in the cycles for different mass loadings are plotted in Fig. 5b. As the mass loading increases, the specific capacity of Si/RGO composite electrode still maintains at a relatively high level (~2300 mAh/g at 6 A/g, based on the mass of SiNPs), which confirms that the layer-by-layer Si/RGO nanocomposite structure can well utilize the active materials in electrodes for electrochemical reactions. As expected, the areal capacity increases with the mass loading, e.g. areal capacities increase from 0.22 mAh/cm^2 for the mass loading of 0.1 mg/cm^2 to 1.50 mAh/cm^2 for the mass loading of 1.0 mg/cm^2. The mass loading can be further increased to meet the requirements for higher areal capacity. Similarly, the maximum specific capacity and the corresponding areal capacity in the cycles for different mass loadings at a higher charge/discharge rate of 15 A/g are plotted in Fig. S8. A high specific capacity (~1900 mAh/g) can be still achieved at 15 A/g, indicating a good rate performance of the Si/RGO composite electrode. Fig. 5c displays the voltage profiles of Si/RGO composite electrodes cycled at different galvanostatic charge/discharge rates, i.e. current densities. For a slow cyclic rate of 0.6A/g, the discharge capacity of Si/RGO composite electrode reaches 3170 mAh/g, close to the theoretical capacity of the active material SiNPs (~3600 mAh/g). Usually, for conventional Si- or graphite-based electrodes, the achievable capacity would significantly decrease as the charge/discharge current density increases, mainly due to the slow kinetics of lithiation/delithiation, ohmic polarization or Li plating. However, our Si/RGO composite

electrode can retain a high capacity even under a fast charge/discharge. It delivers the first cycle capacity of 2173 mAh/g at 6 A/g and 1756 mAh/g at 15 A/g. The maximum achievable capacity can be further increased once all the SiNPs are electrochemically activated. The voltage profiles of Si/RGO composite electrodes in 1st, 20th and 200th cycles under a current density of 6 A/g are plotted in Fig. 5d. The capacity gradually increases to 2422 mA h/g after 20th cycles, due to the gradual electrochemical activation of SiNPs at the early cycling. This high achievable capacity during fast charge/discharge indicates that the Si/RGO composite electrodes has a superior rate performance and therefore can be used for the applications with an extra high charge/-discharge requirement. In additional to the excellent rate performance, the Si/RGO composite electrode shows a good reversibility. After 200 cycles, the discharge capacity slightly decreases to 1849 mAh/g, corresponding to a good capacity retention of 85% with respect to the capacity in the first cycle (Fig. 5d).

The outstanding rate performance and excellent reversibility of Si/RGO composite electrode are also confirmed by the long-term capacity retention curve in Fig. 5e. When cycled at a high charge/discharge rate of 15 A/g, the Si/RGO composite electrode delivers a maximum capacity of 1956 mAh/g and can be cycled for 1000 cycles with a 71.3% retention of the first cycle capacity. In a control experiment, the slurry-cast SiNPs electrodes (50% SiNPs, 25% SuperP carbon and 25% CMC, by weight) exhibits a sharp decline in capacity when even operated under a much lower current density of 0.5 A/g, Fig. 5e. Another excellent performance of Si/RGO composite electrode is its high coulombic efficiency (CE), which is usually difficult to achieve for the conventional Si-based electrode because of the repetitive SEI formation and breakage associated with the huge volume change [43]. As shown in Fig. 5e, after the initial electrochemical activation, the CE of Si/RGO composite electrode can maintain at a high level around 99% for over 1000 cycles. However, the CE of slurry-based SiNPs electrodes exhibits a huge variation from 94% to 100% during the cycles. The high CE of Si/RGO composite electrode is ascribed to its characteristic nanostructure. The SiNPs are tightly enwrapped by the graphene sheets to form the SiNPs clusters, lowering the surface area exposed to the electrolyte and therefore reducing the side reactions. Meanwhile, the graphene sheets covering the surface of SiNPs clusters have a good chemical and structural stability, which helps form the stable SEI film. These are well supported by the morphology of lithiated and delithiated Si/RGO composite electrode in Fig. 3e–g.

To understand the influence of high strain rate LS compression on the electrochemical performance of Si/RGO composite electrode, we compare the electrochemical performance of the Si/RGO composite electrodes with (red curves) and without (black curves) LS compression in Fig. 6a–c. First, the CV and initial charge/discharge curves of the Si/RGO composite electrode after LS compression in Fig. S9 confirms that the LS treatment does not change the chemical composition and electrochemical properties of active materials in the electrode. All the

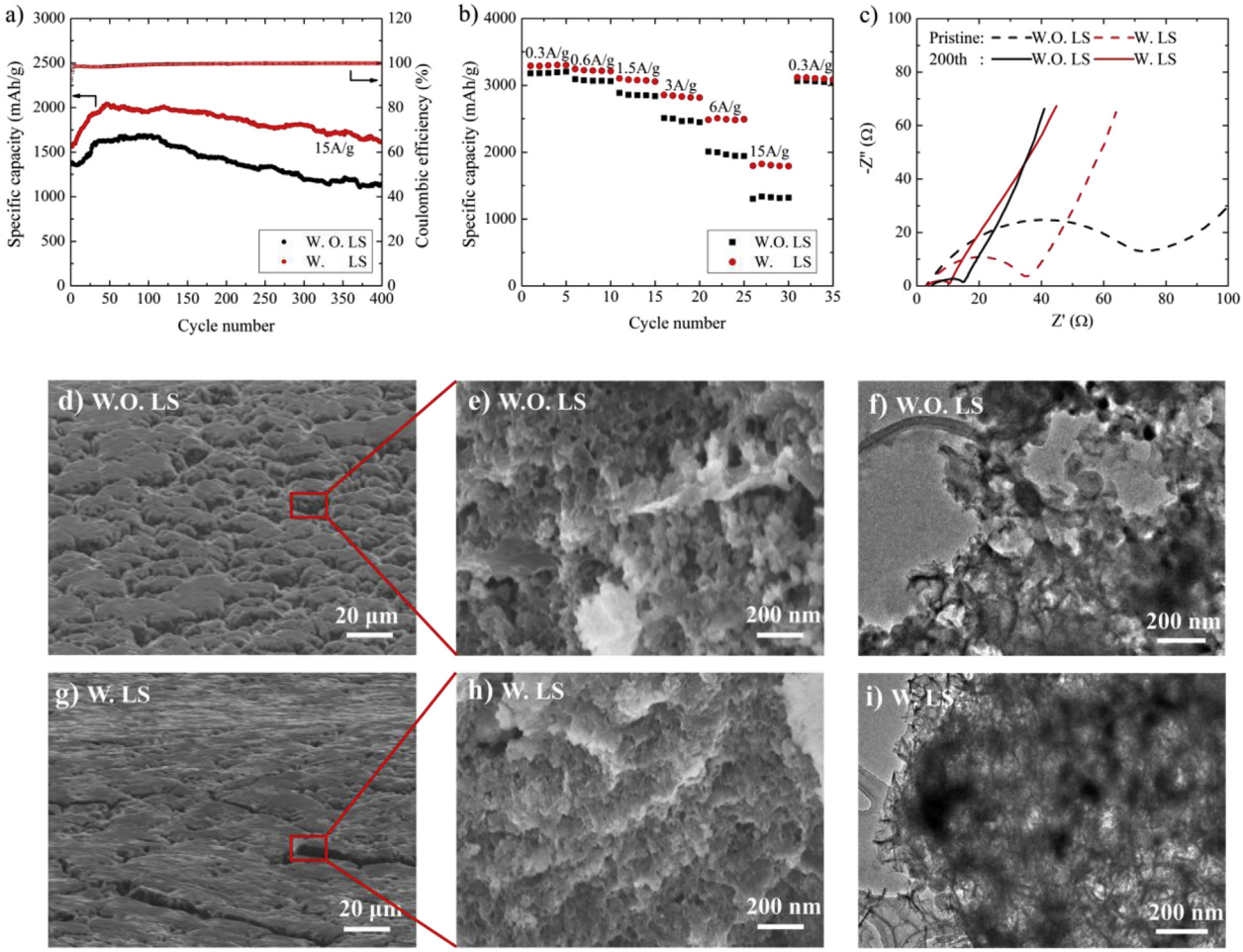

Fig. 6. Comparisons of a) cycling and b) rate performance of Si/RGO composite electrodes with (red) and without (black) LS treatment, and c) the corresponding Nyquist plots of Si/RGO composite electrodes before cycling (dash) and after 200 cycles (solid), respectively. Electrochemical impedances of the Si/RGO composite electrodes with and without LS treatment are extracted from the Nyquist plots. d-i) SEM and TEM observation on the morphology of after-cycles (200 cycles) Si/RGO composite electrodes. d) SEM of non-treated electrode (lithiated); e) Zoom-in SEM of delithiated non-treated Si/RGO composite; f) TEM observation of non-treated Si/RGO composite electrode; g) SEM of LS-treated electrode (lithiated); h) Zoom-in SEM of delithiated LS-treated Si/RGO composite electrode; i) TEM observation of LS-treated Si/RGO composite electrode. (For interpretation of the references to color in this figure legend, the reader is referred to the Web version of this article.)

cathodic and anodic peaks of LS treated Si/RGO composite electrode are in good agreement with that of SiNPs. Fig. 6a shows the cycling performance at 15 A/g for the Si/RGO composite electrodes with (red) and without (black) LS compression. Both the LS-treated and non-treated electrodes show a relatively good electrochemical stability. However, the LS-treated electrodes deliver a higher capacity of 2040 mAh/g in the fast charge/discharge than that of non-treated electrodes (1690 mAh/g). It indicates the LS compression could improve the rate performance of the Si/RGO composite electrode. Fig. 6b shows the rate capacities of LS-treated and non-treated electrodes for the varied charge/discharge current densities from 0.3 A/g to 15 A/g. The capacity gradually decreases along with the increase of the current density, while almost recovers to the initial value once the current density goes back to 0.3 A/g. Comparison on capacities of the LS-treated and non-treated electrodes clearly shows the improvement of rate performance induced by the LS compression. When Si/RGO composite electrodes are cycled with a low current density of 0.3 A/g, the LS-treated and non-treated electrodes have close specific capacities of 3292 mAh/g and 3177 mA/g, respectively. When current density is increased, the difference of capacity between LS-treated and non-treated electrodes becomes obvious. For a high current density of 15 A/g, specific capacity of the LS-treated electrode is 40% higher than that of the electrode without LS compression. The improved rate performance by the LS treatment can be well explained by the characteristic nanostructures of Si/RGO composite electrodes after LS compression, as shown in Figs. 1f and Fig. 3a–h. The graphene sheets that tightly enwrap the SiNPs clusters provide a fast electrons path due to their high electron conductivity, and the strain induced graphene pores create the out-of-plane diffusion channels for Li ions, both of which contribute to a fast kinetic of lithiation and delithiation during battery cycling. Electrochemical impedance spectroscopy (EIS) measurement in Fig. 6c also confirms that the LS-treated electrode has a lower electrochemical impedance in both pristine and cycled state, which is in a good agreement with the characteristic nanostructures and the excellent rate performance of LS-treated electrode.

Note that the improvement of rate performance from the LS compression is significantly regulated by the laser power density. A too low laser power density (27.5 MW/cm^2), as expected, has no effect on the rate performance of the Si/RGO nanocomposite electrodes while a too high laser power density (110 MW/cm^2) seems to deteriorate the overall performance of the electrodes, presumably due to the serious damage of the layer structure induce by the high laser power, Fig. S10. Mechanical calendaring is another common way to improve the contact conditions between conductive matrix and active materials in the conventional slurry-cast electrodes, however, in a control experiment, we find that the mechanical calendaring (~120 MPa hydrostatic pressure) shows a very limited influence on the performance of Si/RGO composite electrodes, Fig. S11. The reason is that the quasi-static mechanical compression can only apply a much lower strain rate (~10^6 s^{-1} for LS compression) on the Si/RGO composite electrodes, which is not able to plastically deform the SiNPs or graphene to form the characteristic nanostructures.

We also study the after-cycle morphology of the LS-treated and non-treated Si/RGO composite electrodes in Fig. 6d–i. Fig. 6d&g give a general comparison of the after-cycle morphology between the LS-treated and non-treated Si/RGO electrode, both in lithiated states. For the non-treated Si/RGO (Fig. 6d), the electrode film tends to form separated islands of around 10 μm in size, leaving large cracks in between. While for the LS-treated Si/RGO (Fig. 6g), the electrode shows an excellent mechanical integrity with only a few narrow cracks, due to the improved interfacial contact between Si–Si and Si-G. It has already been shown in the previous section that the Si/RGO composite will transform into a mesoporous state after delithiation. A comparison between the lithiated (solid) and delithiated (mesoporous) Si/RGO composite is shown in Fig. S12. It is likely that such transition affects the mechanical integrity of the electrode. Fig. 6e shows the delithiated state of a non-treated Si/RGO composite electrode. Loose contact or even delamination are prone to occur at the Si-G interfaces, since the graphene edges are distinctly exposed. However, the morphology of a delithiated LS-treated Si/RGO composite electrode shown in Fig. 6h indicates that the mesoporous silicon exhibits a finer and denser texture. Such microstructure explains the lower electrochemical impedance of LS-treated Si/RGO composite electrode compared to the non-treated one. Also, the graphene edges are hardly seen; this can be that the well integration between SiNPs and graphene remains throughout the entire electrochemical cycles. Lastly, the after-cycle electrode is broken by sonication and inspected by TEM. Fig. 6f showed a typical fragment of after-cycle non-treated Si/RGO composite. The SiNPs and graphene components within the composite are separated and randomly fragmented by the sonication process. While in Fig. 6i, the after-cycle LS-treated Si/RGO composite shows well integrated SiNPs and graphene network even after sonication. Fig. S13 shows zoom-in views of the graphene frame and the mesoporous SiNPs respectively. Likely, the mechanically robust graphene network is able to contain the mesoporous SiNPs within its rich internal space. Such mechanism is showing that the nanoscale interfacial enhancement brought by LS compression process is the key in improving the mechanical stability of the Si/RGO composite electrode, which in turn could play an important role in maintain the mechanical integrity of electrode during electrochemical cycles. Fig. S14 shows the after-cycle thickness of the non-treated and LS-treated electrodes. The original thicknesses of these Si/RGO electrodes are 7.3 μm without LS and 4.4 μm with LS. The thicknesses after cycling are 25 μm for non-treated electrodes and 22 μm for LS-treated electrodes. For the LS-treated electrodes, the volume expansion is 500%, higher than the theoretical volume expansion (400%) of silicon electrode. This means that the porosity of the lithiated electrode increased during electro-chemical cycles, compared to the initial state of the Si/RGO electrode. The extra volume within the electrode are possibly filled with electrolyte and SEI layers.

2.3. Electrochemical performance of full-cell with NMC cathode & Si/RGO anode

A prototype full-cell is built to demonstrate the commercial viability of our Si/RGO composite electrodes. The Si/RGO composite anode with a mass loading of 0.5 mg/cm^2 is paired with a slurry-cast $LiNi_{0.6}Mn_{0.2}Co_{0.2}O_2$ (NMC) cathode with a mass loading of 7 mg/cm^2, to form the full-cell. Fig. 7a plots the cyclic performance of NMC&Si/RGO full-cell at a charge/discharge rate of 0.25 mA/cm^2 and 1.0 mA/cm^2 in a voltage window from 2 V to 4.3 V. The NMC&Si/RGO full-cell delivers a good areal capacity of 0.95 mAh/cm^2 at a charge/discharge rate of 0.25 mA/cm^2 and 0.70 mAh/cm^2 at 1 mA/cm^2. Due to the formation of the initial SEI layer in the first cycle, the initial columbic efficiency is 73% (Fig. S15). This full cell displayed an excellent cycle performance with 98% capacity retention after 50 cycles at 0.25 mA/cm^2, and a high energy density of 467 Wh/kg with an average voltage of ~3.58 V, Fig. 7a and b. The volumetric energy density of the NMC&Si/RGO full cell is calculated to be 1751 Wh/L, based on the thickness of 5 μm for anode and 21 μm for cathode. Fig. 7c plots the capacity retention of the NMC&Si/RGO full-cell, NMC&Li half-cell, and Si/RGO&Li half-cell at various charge/discharge rate from 0.1 mA/cm^2 to 2 mA/cm^2. The full-cell maintains a 79.6% capacity retention when the current density increases from 0.1 mA/cm^2 to 2 mA/cm^2. Accordingly, the power density of NMC & Si/RGO full-cell reaches 808 W/kg. This high-power density is attributed to the good rate performance of both NMC cathode and Si/RGO composite anode. NMC (especially $LiNi_{0.6}Mn_{0.2}Co_{0.2}O_2$) cathode is known as its excellent rate performance (Fig. 7c), while conventional graphite anode would experience serious issues during the fast charge/discharge such as Li plating, which significantly limits the performance of NMC/Graphite full-cell during fast charge/discharge [44,45]. As proven by Figs. 5 and 7c, our Si/RGO composite anode shows an excellent rate performance which can well pair with NMC cathode and thus allows the NMC&Si/RGO full-cell to better survive from a high charge/discharge current density. The voltage profiles of NMC&Si/RGO full-cell at various charge/discharge rates from 0.1 mA/cm^2 to 2.0 mA/cm^2 in Fig. 7d also

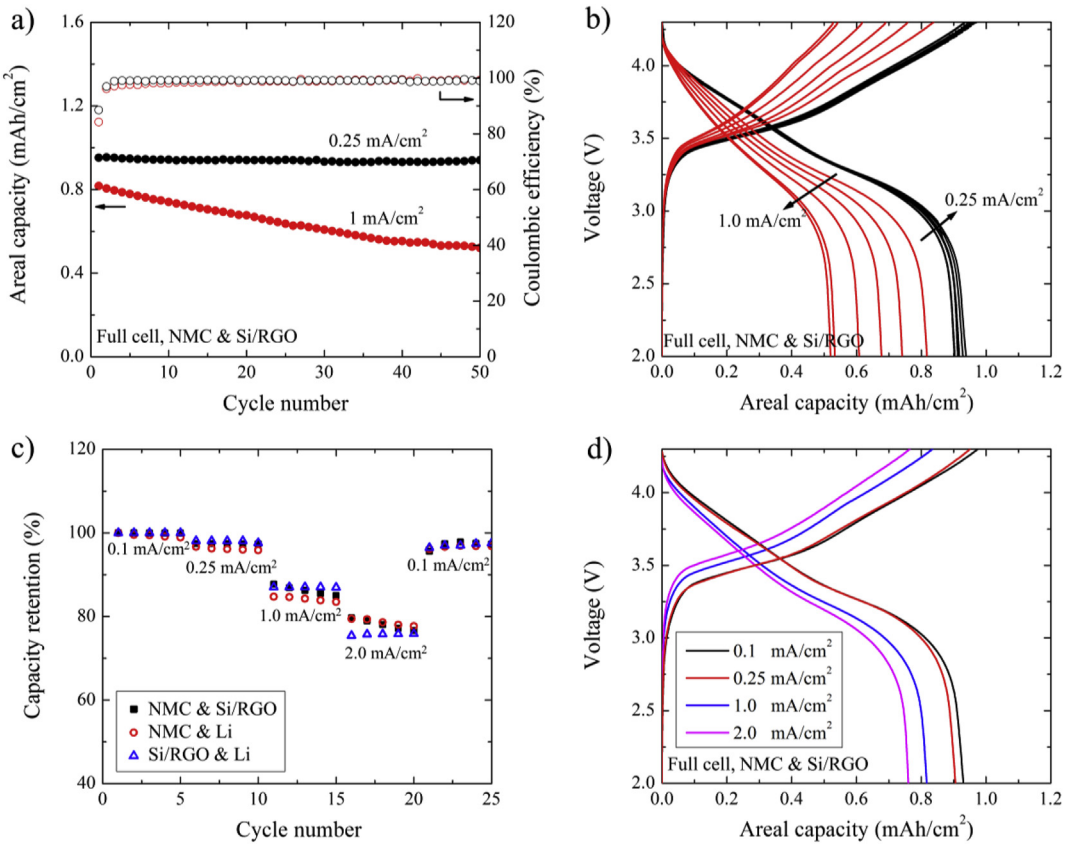

Fig. 7. a) Cyclic performance and b) charge-discharge curves of NMC&Si/RGO full-cell at a charge/discharge rate of 0.25 mA/cm^2 and 1.0 mA/cm^2. c) Capacity retentions of NMC&Si/RGO full-cell, NMC&Li half-cell, and Si/RGO&Li half-cell at various charge/discharge rates from 0.1 mA/cm^2 to 2.0 mA/cm^2. d) Charge-discharge curves of NMC&Si/RGO full-cell at various charge/discharge rates from 0.1 mA/cm^2 to 2.0 mA/cm^2.

confirm that the full cell does not experience serious electrochemical issues during the fast charge/discharge.

3. Conclusion

In summary, a novel manufacturing method combining roll-to-roll coating process and laser shock compression process towards Si/RGO composite LIB anode has been developed. The resultant layer-by-layer structured electrodes show an outstanding capacity of 1956 mAh/g at the high current density of 15 A/g. The high capacity at high current density is able to retain 71.3% after 1000 cycles. The improved electrochemical performance is attributed to the uniform and stable layer-by-layer structure, the improved nanoscale interfaces and the dense nanoscale pores on RGO sheets. These merits are the direct consequences of our manufacturing process, especially the synergy between the nanoscale heterogeneous layers and the high strain-rate laser shock compression. For future work, the addition of nano-binders or surface modifications could further improve the Si/RGO electrode under the presented manufacturing process.

3.1. Experimental details

Dispersion preparation. 0.2 g Si NPs (NanoAmor, #0143KE, 50–80 nm dia.) and 1 g polyvinylpyrrolidone (PVP) (Sigma Aldrich, PVP10) are added to 20mL ethanol. With a magnetic stirring, the solution is left at 70 °C overnight for PVP capping. Then, the capped SiNPs are centrifuged and rinsed with ethanol for 3 times to remove the excessive dissolved PVP, leaving stable 10 mg/mL SiNPs dispersion in ethanol. Finally, the dispersion is diluted to 4 mg/mL for gravure roller coating. 10 mg/mL graphene oxide (Cheap Tubes, #060102) aqueous dispersion is made by sonication for 2 h. Before rod coating, the dispersion is diluted with ethanol to 1.5 mg/mL, additional sonication might be needed depending on the homogeneity of the dispersion. It is assumed that the weights of Si and RGO in the electrode are proportional to the concentrations of their coating dispersion.

Laser-shock (LS) assisted manufacture of layer-by-layer Si/RGO electrodes. Mirwec Mini-Labo Deluxe R2R coater (Fig. 1c) is used for the Si/RGO layer-by-layer coating [46]. Microgravure R90 is used; and approximately 12 μm of wet film is coated each roll. Rolling speed is set to 1 m/min. The SiNP solution and the GO solution are alternatingly coated onto the copper foil to form a layer-by-layer composite, by substituting the solution and rewinding the roll. Since alcoholic solution is used, the drying of the coating takes only a few seconds. This coating process for each solution is repeated till the ideal mass loading is reached. Typically, loading of 0.5 mg/cm^2 requires 80 layers of SiNPs and 81 layers of RGO; loading of 1.0 mg/cm^2 requires 160 layers of SiNPs and 161 layers of RGO. The final loading of the composite electrode is up to 1.0 mg/cm^2. The as-coated electrode shows a brownish color. The foil of electrode is punched into disks of 13 mm in diameter. These disks are then transferred to LS treatment. When the LS process is performed, the electrode disk is placed beneath the sacrificial copper foil, then clamped by two BK7 glass pieces. A laser pulse (1064 nm wavelength, 7 ns pulse duration) is applied ono the sacrificial layer, generating a shock wave propagating onto the electrode. As a result, the Si/RGO composite electrode is compressed by the LS. The detail effect and mechanism of the LS process is discussed in our past work. Finally, the electrodes are transferred to furnace annealing at 600 °C for 2 h under protection of argon atmosphere. It is worth noting that at higher temperatures, the annealing process would cause the copper foil beneath the electrode to curve.

Material Characterizations. Scanning electron microscope (SEM) and transmission electron microscopy (TEM) images are taken using a Hitachi s-4800 FESEM and a FEI Tecnai G2 20 TEM, respectively.

Mechanical strength of the samples is obtained by nanoindentation measurement (G200, Keysight Technologies). Standard Oliver and Pharr method [47] is used to get the nanohardness and elastic modulus of the materials from the force-displacement curves. Indentations with maximum depth of 250 nm are conducted. The loading, holding, and unloading times are 20, 5, and 20 s, respectively. Surface morphology of the samples are measured by Bruker GT-K optical profilometer using 50X interferometric objective. Surface texture are measured by the B46.1 - 2009 Standard [48].

Molecular dynamic (MD) modeling. MD modeling is performed using LAMMPS. The adaptive intermolecular reactive empirical bond order (AIREBO) potential is used for graphene [49]. The cutoff distance is 2.0 Å. The interactions between SiNPs and graphene have been modeled using Lennard-Jones potential [50]. The system is calculated in ensemble NVT (Nose–Hoover thermostat) with the temperature maintained at 300 K. The time step is 1 fs. The laser shock is applied on a thin layer of rigid impactor Cu film on the top of the sacrificial Cu film of 25 nm. MD simulation has been done in two stages: First, the model is implemented by isothermal–isobaric ensemble for 1 ps with periodic boundary condition in all directions to reach equilibrium state. Second, impactor atoms are applied with a laser shock. To generate a shock wave, a velocity of 100 m/s is applied to the impactor Cu film, which corresponds to laser pressure of 0.6 GPa. This value is calculated based on literature [51]. Graphene monolayers used in this model contain structural imperfections, such as Stone–Thrower–Wales (STW) defect, single- and di-vacancies and nano voids. These defects are spread on the graphene randomly by introducing 2% atomic vacancies.

Electrochemical measurements. As-annealed electrodes are stored in an argon-filled glovebox (moisture and oxygen levels less than 0.5 ppm) for several days before use. Electrodes are assembled into CR-2032 type coin cells for electrochemical testing. For the half-cell assembling, the Si/RGO composite electrode, Li foil, and Celgard-2502 membrane are used as the cathode, anode, and separator, respectively. The electrolyte is composed of 1.2 M $LiPF_6$ salt dissolved in ethylene carbonate/diethyl (EC/DEC, 1:1, vol%; Sigma Aldrich) with 10% fluoroethylene carbonate (FEC, Alfa Aesar). All assembled cells are placed to rest overnight to ensure complete wetting before electrochemical tests. Electrochemical cyclic tests are carried out using a battery testing system (BT-2043, Arbin Instruments). Cyclic voltammetry (CV) with the voltage window of 0.01∼1.5V vs. Li/Li^+ and scan rate of 0.1 mV/s is performed to analyze the electrochemical characteristics of the Si/RGO composite electrode. Galvanostatic cycling in a voltage range between 0.01 and 1.0 V is performed to evaluate the cyclic performance of the Si/RGO composite electrode. Electrochemical impedance spectroscopy (EIS) measurements are carried out using an impedance analyzer (Versa STAT 3, Princeton Applied Research). The amplitude voltage and frequency range are set as 5 mV and 0.1 Hz–100 kHz. All the electrochemical measurements are conducted at room temperature. The full-cells are assembled by pairing the $LiNi_{0.6}Mn_{0.2}Co_{0.2}O_2$ (NMC) cathode and Si/RGO composite anode with the areal capacities of 1.1 mAh/cm^2 and 1.2 mAh/cm [2], respectively, corresponding to a N/P ratio of ∼1.1. NMC cathode is fabricated by casting slurry on an Al current collector [52]. Commercialized $LiNi_{0.6}Mn_{0.2}Co_{0.2}O_2$ powder (MSE supplies LLC), Super P carbon (MTI co.) and polyvinylidene fluoride (PVDF, MTI co.) binder with the weight ratio of 90:5:5 are mixed in the N-methyl-2-pyrrolidone (NMP, Sigma Aldrich) solvent to form the slurry. The areal loading of the NMC cathode is ∼7 mg/cm^2. The as-coated NMC electrodes are dried at 110 °C in a vacuum oven overnight. CR-2032 type coin cells are assembled using the same procedure as that of the half-cell above. Galvanostatic cycling test of the full cell is carried out in the voltage window between 2.0 and 4.3 V.

Acknowledgements

K. Z. and G. J. C acknowledge the support by the Office of Naval Research's NEPTUNE Program under the grant number N00014-16-1-3109. K. Z. also acknowledges the support by the National Science Foundation through the grant CBET-1603866. G. J. C acknowledges the support by the National Science Foundation CMMI NanoManufacturing Program.

Appendix A. Supplementary data

Supplementary data to this article can be found online at https://doi.org/10.1016/j.ensm.2019.07.019.

References

[1] B. Scrosati, J. Garche, Lithium batteries: status, prospects and future, J. Power Sources 195 (9) (2010) 2419–2430.
[2] C.-Y. Chen, T. Sano, T. Tsuda, K. Ui, Y. Oshima, M. Yamagata, et al., In situ scanning electron microscopy of silicon anode reactions in lithium-ion batteries during charge/discharge processes, Sci. Rep. 6 (2016) 36153.
[3] C. Li, T. Shi, H. Yoshitake, H. Wang, Improved performance in micron-sized silicon anodes by in situ polymerization of acrylic acid-based slurry, J. Mater. Chem. A 4 (43) (2016) 16982–16991.
[4] C.Y. Chen, A. Sawamura, T. Tsuda, S. Uchida, M. Ishikawa, S. Kuwabata, Visualization of Si anode reactions in coin-type cells via operando scanning electron microscopy, ACS Appl. Mater. Interfaces 9 (41) (2017) 35511–35515.
[5] T. Yoon, C.C. Nguyen, D.M. Seo, B.L. Lucht, Capacity fading mechanisms of silicon nanoparticle negative electrodes for lithium ion batteries, J. Electrochem. Soc. 162 (12) (2015) A2325–A2330.
[6] C. Shen, M. Ge, L. Luo, X. Fang, Y. Liu, A. Zhang, et al., In situ and ex situ TEM study of lithiation behaviours of porous silicon nanostructures, Sci. Rep. 6 (2016) 31334.
[7] X.H. Liu, L. Zhong, S. Huang, S.X. Mao, T. Zhu, J.Y. Huang, Size-dependent fracture of silicon nanoparticles during lithiation, ACS Nano 6 (2) (2012) 1522–1531.
[8] M. Ko, S. Chae, J. Ma, N. Kim, H.-W. Lee, Y. Cui, et al., Scalable synthesis of silicon-nanolayer-embedded graphite for high-energy lithium-ion batteries, Nat. Energy 1 (2016) 16113.
[9] D. Lin, Z. Lu, P.-C. Hsu, H.R. Lee, N. Liu, J. Zhao, et al., A high tap density secondary silicon particle anode fabricated by scalable mechanical pressing for lithium-ion batteries, Energy Environ. Sci. 8 (8) (2015) 2371–2376.
[10] Z. Chen, C. Wang, J. Lopez, Z. Lu, Y. Cui, Z. Bao, High-areal-capacity silicon electrodes with low-cost silicon particles based on spatial control of self-healing binder, Adv. Energy Mater. 5 (8) (2015) 1401826.
[11] Z. Wang, H. Gao, Q. Zhang, Y. Liu, J. Chen, Z. Guo, Recent advances in 3D graphene architectures and their composites for energy storage applications, Small 15 (3) (2019) 1803858.
[12] D. Lin, Y. Liu, Z. Liang, H.-W. Lee, J. Sun, H. Wang, et al., Layered reduced graphene oxide with nanoscale interlayer gaps as a stable host for lithium metal anodes, Nat. Nanotechnol. 11 (2016) 626.
[13] L. Ji, H. Zheng, A. Ismach, Z. Tan, S. Xun, E. Lin, et al., Graphene/Si multilayer structure anodes for advanced half and full lithium-ion cells, Nano Energy 1 (1) (2012) 164–171.
[14] F.-Y. Su, Y.-B. He, B. Li, X.-C. Chen, C.-H. You, W. Wei, et al., Could graphene construct an effective conducting network in a high-power lithium ion battery? Nano Energy 1 (3) (2012) 429–439.
[15] P. Nie, Z. Le, G. Chen, D. Liu, X. Liu, H.B. Wu, et al., Graphene caging silicon particles for high-performance lithium-ion batteries, Small 14 (25) (2018), e1800635.
[16] L. Fei, S.H. Yoo, R.A. Villamayor, B.P. Williams, S.Y. Gong, S. Park, et al., Graphene oxide involved air-controlled electrospray for uniform, fast, instantly dry, and binder-free electrode fabrication, ACS Appl. Mater. Interfaces 9 (11) (2017) 9738–9746.
[17] C. Shan, K. Wu, H.J. Yen, C. Narvaez Villarrubia, T. Nakotte, X. Bo, et al., Graphene oxides used as a new "dual role" binder for stabilizing silicon nanoparticles in lithium-ion battery, ACS Appl. Mater. Interfaces 10 (18) (2018) 15665–15672.
[18] C. Wu, J. Lin, R. Chu, J. Zheng, Y. Chen, J. Zhang, et al., Reduced graphene oxide as a dual-functional enhancer wrapped over silicon/porous carbon nanofibers for high-performance lithium-ion battery anodes, J. Mater. Sci. 52 (13) (2017) 7984–7996.
[19] M. Zhou, X. Li, B. Wang, Y. Zhang, J. Ning, Z. Xiao, et al., High-performance silicon battery anodes enabled by engineering graphene assemblies, Nano Lett. 15 (9) (2015) 6222–6228.
[20] D. Liao, X. Kuang, J. Xiang, X. Wang, A silicon anode material with layered structure for the lithium-ion battery, J. Phys. Conf. Ser. 986 (2018) 012024.
[21] L. Jiao, Z. Sun, H. Li, F. Li, T. Wu, L. Niu, Collector and binder-free high quality graphene film as a high performance anode for lithium-ion batteries, RSC Adv. 7 (4) (2017) 1818–1821.
[22] C. Chen, M. Wu, S. Wang, J. Yang, J. Qin, Z. Peng, et al., An in situ iodine-doped graphene/silicon composite paper as a highly conductive and self-supporting electrode for lithium-ion batteries, RSC Adv. 7 (61) (2017) 38639–38646.
[23] H. Yue, Q. Li, D. Liu, X. Hou, S. Bai, S. Lin, et al., High-yield fabrication of graphene-wrapped silicon nanoparticles for self-support and binder-free anodes of lithium-ion batteries, J. Alloy. Comp. 744 (2018) 243–251.
[24] J. Qin, M. Wu, T. Feng, C. Chen, C. Tu, X. Li, et al., High rate capability and long cycling life of graphene-coated silicon composite anodes for lithium ion batteries, Electrochim. Acta 256 (2017) 259–266.

[25] J. Chang, X. Huang, G. Zhou, S. Cui, P.B. Hallac, J. Jiang, et al., Multilayered Si nanoparticle/reduced graphene oxide hybrid as a high-performance lithium-ion battery anode, Adv. Mater. 26 (5) (2014) 758–764.
[26] Y. Li, K. Yan, H.-W. Lee, Z. Lu, N. Liu, Y. Cui, Growth of conformal graphene cages on micrometre-sized silicon particles as stable battery anodes, Nat. Energy 1 (2016) 15029.
[27] M.V. Shelke, H. Gullapalli, K. Kalaga, M.-T.F. Rodrigues, R.R. Devarapalli, R. Vajtai, et al., Facile synthesis of 3D anode assembly with Si nanoparticles sealed in highly pure few layer graphene deposited on porous current collector for long life Li-ion battery, Adv. Mater. Interfaces 4 (10) (2017) 1601043.
[28] M. Ko, S. Chae, S. Jeong, P. Oh, J. Cho, Elastic a-silicon nanoparticle backboned graphene hybrid as a self-compacting anode for high-rate lithium ion batteries, ACS Nano 8 (8) (2014) 8591–8599.
[29] H. Wu, G. Yu, L. Pan, N. Liu, M.T. McDowell, Z. Bao, et al., Stable Li-ion battery anodes by in-situ polymerization of conducting hydrogel to conformally coat silicon nanoparticles, Nat. Commun. 4 (2013) 1943.
[30] J. Zhao, G. Zhou, K. Yan, J. Xie, Y. Li, L. Liao, et al., Air-stable and freestanding lithium alloy/graphene foil as an alternative to lithium metal anodes, Nat. Nanotechnol. 12 (2017) 993.
[31] L. Li, Z. Zuo, H. Shang, F. Wang, Y. Li, In-situ constructing 3D graphdiyne as all-carbon binder for high-performance silicon anode, Nano Energy 53 (2018) 135–143.
[32] D. Das, S. Kim, K.-R. Lee, A.K. Singh, Li diffusion through doped and defected graphene, Phys. Chem. Chem. Phys. 15 (36) (2013) 15128–15134.
[33] N. Kim, C. Oh, J. Kim, J.-S. Kim, E.D. Jeong, J.-S. Bae, et al., High-performance Li-ion battery anodes based on silicon-graphene self-assemblies, J. Electrochem. Soc. 164 (1) (2016) A6075–A6083.
[34] J. Luo, X. Zhao, J. Wu, H.D. Jang, H.H. Kung, J. Huang, Crumpled graphene-encapsulated Si nanoparticles for lithium ion battery anodes, J. Phys. Chem. Lett. 3 (13) (2012) 1824–1829.
[35] Y. Miroshnikov, G. Grinbom, G. Gershinsky, G.D. Nessim, D. Zitoun, Do we need covalent bonding of Si nanoparticles on graphene oxide for Li-ion batteries? Faraday Discuss 173 (0) (2014) 391–402.
[36] S. Basu, S. Suresh, K. Ghatak, S.F. Bartolucci, T. Gupta, P. Hundekar, et al., Utilizing van der Waals slippery interfaces to enhance the electrochemical stability of silicon film anodes in lithium-ion batteries, ACS Appl. Mater. Interfaces 10 (16) (2018) 13442–13451.
[37] X. Zhao, C.M. Hayner, M.C. Kung, H.H. Kung, In-plane vacancy-enabled high-power Si-graphene composite electrode for lithium-ion batteries, Adv. Energy Mater. 1 (6) (2011) 1079–1084.
[38] P. Chang, X. Liu, Q. Zhao, Y. Huang, Y. Huang, X. Hu, Constructing three-dimensional honeycombed graphene/silicon skeletons for high-performance Li-ion batteries, ACS Appl. Mater. Interfaces 9 (37) (2017) 31879–31886.
[39] D. Lin, M. Saei, S. Suslov, S. Jin, G.J. Cheng, Super-strengthening and stabilizing with carbon nanotube harnessed high density nanotwins in metals by shock loading, Sci. Rep. 5 (2015) 15405.
[40] D. Lin, M. Motlag, M. Saei, S. Jin, R.M. Rahimi, D. Bahr, et al., Shock engineering the additive manufactured graphene-metal nanocomposite with high density nanotwins and dislocations for ultra-stable mechanical properties, Acta Mater. 150 (2018) 360–372.
[41] D. Datta, J. Li, N. Koratkar, V.B. Shenoy, Enhanced lithiation in defective graphene, Carbon 80 (2014) 305–310.
[42] N. Liu, Z. Lu, J. Zhao, M.T. McDowell, H.-W. Lee, W. Zhao, et al., A pomegranate-inspired nanoscale design for large-volume-change lithium battery anodes, Nat. Nanotechnol. 9 (2014) 187.
[43] M.T. McDowell, S. Xia, T. Zhu, The mechanics of large-volume-change transformations in high-capacity battery materials, Extreme Mech. Lett. 9 (2016) 480–494.
[44] S. Wang, M. Yan, Y. Li, C. Vinado, J. Yang, Separating electronic and ionic conductivity in mix-conducting layered lithium transition-metal oxides, J. Power Sources 393 (2018) 75–82.
[45] K.G. Gallagher, S.E. Trask, C. Bauer, T. Woehrle, S.F. Lux, M. Tschech, et al., Optimizing areal capacities through understanding the limitations of lithium-ion electrodes, J. Electrochem. Soc. 163 (2) (2016) A138–A149.
[46] Q. Nian, M. Saei, Y. Hu, B. Deng, S. Jin, G.J. Cheng, Additive roll printing activated cold welding of 2D crystals and 1D nanowires layers for flexible transparent conductor and planer energy storage, Extreme Mech. Lett. 9 (2016) 531–545.
[47] W.C. Oliver, G.M. Pharr, An improved technique for determining hardness and elastic modulus using load and displacement sensing indentation experiments, J. Mater. Res. 7 (6) (1992) 1564–1583.
[48] A. American Standards, C. Sectional Committee on, Designation of Surface Q, American Society of Mechanical E, Society of Automotive E. *Surface Texture : Surface Roughness, Waviness and Lay*, American Society of Mechanical Engineers, New York, 1962.
[49] S.J. Stuart, A.B. Tutein, J.A. Harrison, A reactive potential for hydrocarbons with intermolecular interactions, J. Chem. Phys. 112 (14) (2000) 6472–6486.
[50] Z. Zhang, T. Li, Carbon nanotube initiated formation of carbon nanoscrolls, Appl. Phys. Lett. 97 (8) (2010) 081909.
[51] R. Fabbro, J. Fournier, P. Ballard, D. Devaux, J. Virmont, Physical study of laser-produced plasma in confined geometry, J. Appl. Phys. 68 (2) (1990) 775–784.
[52] R. Xu, L.S. de Vasconcelos, J. Shi, J. Li, K. Zhao, Disintegration of meatball electrodes for $LiNi_x Mn_y Co_z O_2$ cathode materials, Exp. Mech. (2017) 549–559. Medium: ED; Size.